Modeling Light Propagation in Sea Ice

Curtis D. Mobley, Glenn F. Cota, Thomas C. Grenfell, *Associate Member, IEEE*, Robert A. Maffione, W. Scott Pegau, and Donald K. Perovich

Abstract—**This paper outlines the process by which it is possible to begin with the physical properties of sea ice (such as the size distributions of brine pockets and air bubbles), then predict the optical absorption and scattering properties of the ice, and finally use these inherent optical properties in radiative transfer models to predict light propagation within the ice. Each step of this entire process is illustrated by application to a comprehensive data set of sea ice physical and optical properties. Agreement is found between measured and modeled beam spread functions (bsf's), albedos, and transmittances.**

Index Terms— **Beam spread function (bsf), diffusion theory, modeling, radiative transfer, sea ice.**

I. Introduction

THE 1994 Electromagnetic Properties of Sea Ice (EMPOSI) field experiment near Point Barrow, AK, yielded a unique data set of ice physical, electromagnetic, and optical properties [1]. Experiment site 2 was located approximately 200-m offshore in the Beaufort Sea, AK, on shorefast, first-year ice approximately 1.7 m thick. The physical, electromagnetic, and optical properties of this ice are described in [2] and [3].

This paper illustrates how we can start with the ice physical properties and predict the optical absorption and scattering properties of the ice and, in turn, use these optical properties in radiative transfer models to predict light propagation within the ice. For brevity, we discuss only one ice sample from the site 2 data set and one wavelength. The application of the methods presented here to the more extensive analysis of other data and other wavelengths is reserved for the authors' individual papers. The various measurements made at site 2 and used in this paper were made within a few tens of meters of each other in horizontal location and at various times on May 5–7, 1994. Thus, the data are not strictly colocated and simultaneous, and it is implicitly assumed in our analysis that the ice is horizontally homogeneous over the measurement site and temporally stable over the three-day period.

We selected a mid-ice depth of approximately 0.5 m for detailed modeling because the ice physical properties were fairly constant with depth in this region and optical beam spread measurements were available over horizontal paths at that depth. Likewise, a wavelength of 670 nm was selected because that was the wavelength of the laser used in the horizontal beam spread measurements.

TABLE I
SUMMARY OF MEASURED PHYSICAL AND OPTICAL PROPERTIES IN THE ICE INTERIOR

Property	Value
Temperature	-5.7 deg C
Salinity	5.2‰
Density	0.92 Mg m^{-3}
Brine volume	5.5%
Air volume	< 1%
Absorption coefficient at 670 nm for dissolved and particulate matter	0.02 m^{-1}
Albedo at 670 nm, for bare ice	0.48
Transmittance at 670 nm, for bare ice	0.01
Diffuse "sphere" attenuation at 670 nm	0.7 m^{-1}
Horizontal BSF at 670 nm	see Fig. 3

II. The Data Set

Selected values of temperature, salinity, density, and brine pocket volume at site 2 [2] are shown for reference in Table I. The brine pockets had size distributions that are well described by lognormal distributions for the cross-sectional areas (in a horizontal plane) of the brine pockets. The parameters of the distributions are given in [2, Table I], and the distributions are

Manuscript received October 31, 1997; revised June 15, 1998. This work was supported by the Environmental Optics Program of the United States Office of Naval Research under the EMPOSI program. The work of T. C. Grenfell was supported by the Remote Sensing Program.

C. D. Mobley is with Sequoia Scientific, Inc., Mercer Island, WA 98040 USA (e-mail: mobley@sequoiasci.com).

G. F. Cota is with the Center for Coastal Physical Oceanography, Old Dominion University, Norfolk, VA 23508 USA.

T. C. Grenfell is with the Department of Atmospheric Sciences, University of Washington, Seattle, WA 98195 USA.

R. A. Maffione is with the Hydro-Optics, Biology, and Instrumentation Laboratories, Watsonville, CA 95076 USA.

W. S. Pegau is with the College of Oceanographic and Atmospheric Science, Oregon State University, Corvallis, OR 97331 USA.

D. K. Perovich is with the U.S. Army Cold Regions Research and Engineering Laboratory, Hanover, NH 03755 USA.

Publisher Item Identifier S 0196-2892(98)06664-9.

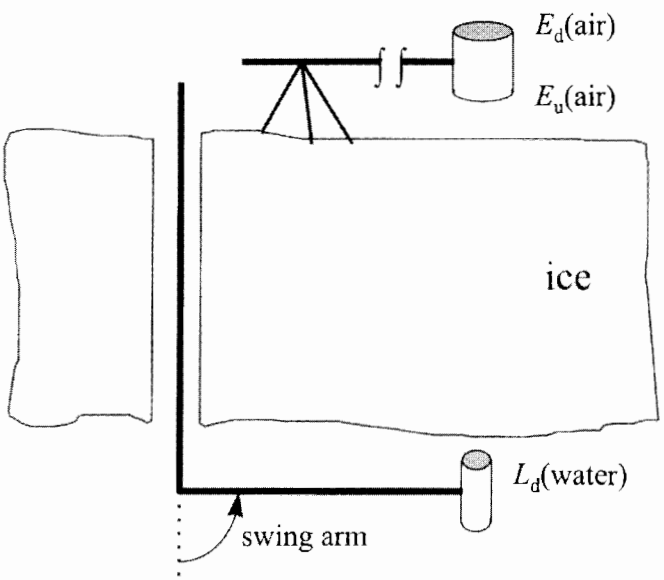

Fig. 1. Schematic layout of the instruments used in measuring ice albedo and transmission.

plotted in [2, Fig. 7]. These data are the foundation for our predictions of ice optical properties.

Optical measurements made at site 2 included the spectral absorption coefficient of dissolved and particulate matter as a function of depth within the ice, spectral albedo of and transmittance through both snow-covered and bare ice, spectral diffuse attenuation as a function of depth within the ice, beam spread functions (bsf's) along horizontal paths at selected depths and path distances within the ice, and bsf's along vertical paths through the ice [3]. A small subset of these measurements, as needed for the discussion below, is given in Table I.

The spectral absorption coefficient for particulate material within the ice was measured on melted ice cores by collecting the particulates on Whatman GF/F glass fiber filters and measuring the absorption in a dual-beam scanning spectrophotometer [4]. The absorption by dissolved matter was determined from the filtrate [5].

The spectral albedo from 400 to 1000 nm was determined by using a tripod-mounted Spectron Engineering SE590 radiometer fitted with a cosine collector to measure the downwelling and upwelling plane irradiances just above the ice surface, E_d(air) and E_u(air), respectively. The albedo is then given by $A = E_u(\text{air})/E_d(\text{air})$. An identical instrument fitted with a radiance detector in an underwater housing and mounted on a swing arm was used to measure the downwelling radiance L_d(water) emerging from the ice into the water. Assuming that the radiance emerging from the ice is isotropic, the downwelling irradiance just beneath the ice is $E_d(\text{water}) = \pi L_d(\text{water})$. The transmittance is $T = E_d(\text{water})/E_d(\text{air})$. Fig. 1 shows this sensor arrangement.

Diffuse attenuation within the ice was measured with a 13-cm-diameter diffusing sphere enclosed between light shields above and below the sphere. This assembly was designed for insertion into the holes used in making the horizontal bsf measurements. This instrument measured an azimuthally averaged irradiance that is weighted toward approximately horizontal directions. The rate of change with depth of this irradiance then yields a diffuse attenuation coefficient K_{sphere} that is particular to the geometry of the collector. However, for sufficient depths within the ice, all diffuse attenuation coefficients approach the same asymptotic value K_∞, and K_{sphere} should then be comparable to any other K function.

The bsf is defined [6] as the irradiance distribution at distance R and angle θ, generated by a narrow collimated beam located at $R = 0$ and emitting light in the $\theta = 0$ direction, normalized by the power of the light source. The irradiance is measured on a surface normal to the radial distance R. As illustrated in Fig. 2, the bsf was measured by drilling two vertical holes a distance R apart in the ice. A pulsed, collimated laser light source was placed in one hole and a cosine irradiance detector in the other, both at the same depth. The bsf was then measured through a full 360° in θ by rotating the source while holding the detector fixed. Phase synchronous detection was used so that the ambient light field within the ice could be subtracted out. The details of these measurements are given in [7]. In the present paper, we use only a small part of the entire bsf data set, namely, the bsf's at one depth (0.45 m) for two hole separations ($R = 0.35$ and 0.68 m). Fig. 3 shows these bsf measurements. To the extent that the ice is uniformly isotropic, the bsf is symmetric about $\theta = 0$. Therefore, for viewing convenience in Fig. 3, we have plotted the bsf for $-180° \le \theta \le 0°$ onto the angle range from $0° \le \theta \le 180°$. The data for $R = 0.68$ m include measurements made for holes both perpendicular and parallel to the ice c axis; the data for $R = 0.35$ m are for holes parallel to the c axis. More extensive presentations of bsf data are given in [3] and [7].

III. Predicting Inherent Optical Properties

Brine pockets in sea ice are usually vertically oriented, irregularly shaped inclusions of varying lengths. Little statistical data are available on the three-dimensional (3-D) structure of brine pockets; even if such data were available, calculations of light scattering by anisotropic, oriented brine pockets would be exceedingly difficult. On the other hand, photomicrographs of ice horizontal thin sections show [2] that the cross-sectional area A of the brine pockets is well described by a lognormal probability distribution function (pdf)

$$\text{pdf}(A) = \frac{1}{\sqrt{2\pi s_A^2}} \frac{1}{A} \exp\left[-\frac{(\ln A - \ln A_m)^2}{2s_A^2}\right]. \quad (1)$$

If the area A is measured in square millimeters, the median area A_m and standard deviation s_A of $\ln A$ for the ice at a depth of 0.75 m at site 2 are $A_m = 0.013$ mm^2 and $s_A = 1.01$. These values of A_m and s_A correspond to a mean brine pocket area of $A_m \exp(s_A^2/2) = 0.023$ mm^2 (see [2, Table I, "first-year ice"]). Fig. 4 shows pdf(A) and the corresponding cumulative distribution function cdf(A) for these parameter values.

To capitalize on these brine pocket statistics and simplify the scattering calculations, a simple model of scattering by brine pockets was used. It was first assumed that the brine pockets can be modeled as vertically oriented prolate spheroids

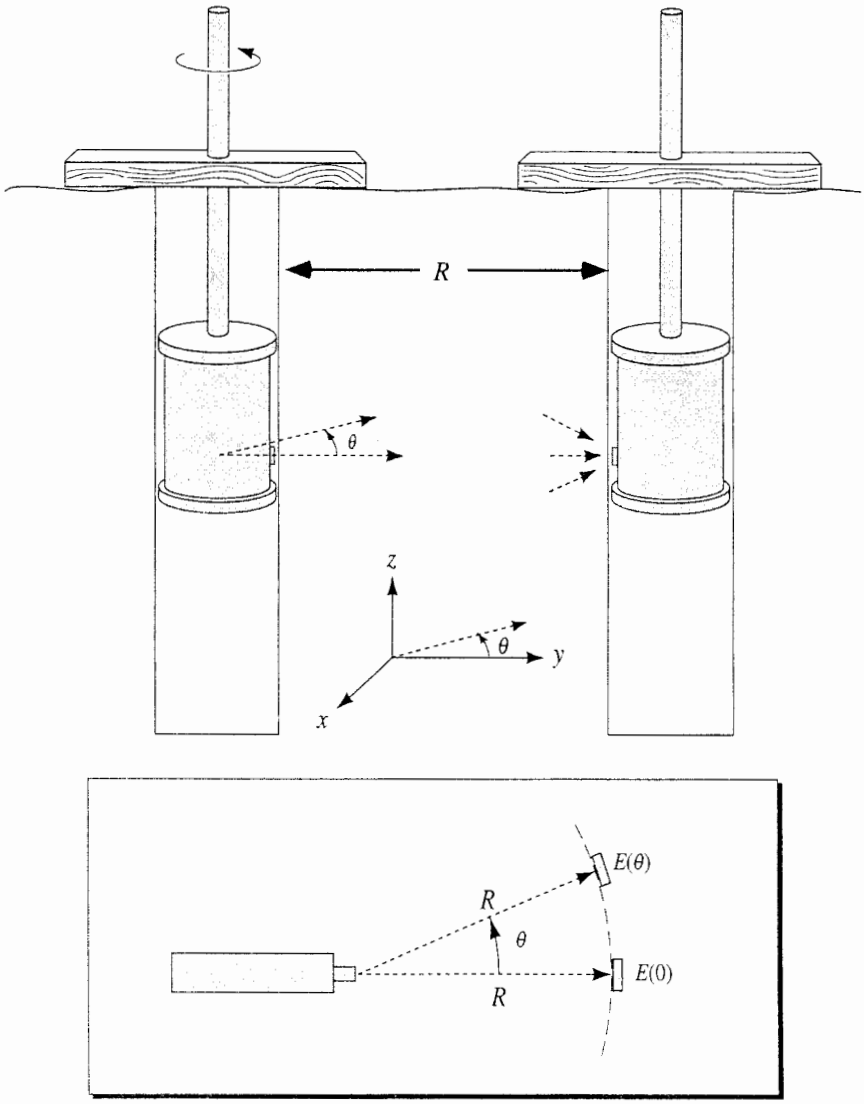

Fig. 2. Schematic layout of the instruments used in measuring the bsf. E is the irradiance measured by a cosine collector.

with a 5:1 ratio of major: minor axes. The median and standard deviation of the cross-sectional areas were then used to determine the corresponding statistics of the minor axes of the prolate spheroids. The prolate spheroids were then converted to equivalent spheres having the same volume-to-surface area as the prolate spheroids. The results are that the median equivalent-sphere radius of a brine pocket is $r_{\mathrm{bp}} = 0.16$ mm and the corresponding standard deviation s_{bp} is 0.51. These equivalent spheres have the same brine volume of 5.5% as was observed. Under the further assumption that these brine pocket equivalent-sphere radii also obey a lognormal size distribution, the A_m and s_A parameters of the area pdf of (1) can be replaced by the corresponding parameters r_{bp} and s_{bp}, respectively, to give the radius pdf. The resulting radius pdf and cdf are plotted in Fig. 4.

Air bubbles were assumed to be spherical and lognormally distributed in size. Measured values for air bubbles in pancake ice (not measured at site 2; see [2, Table I, "pancakes"]) were assumed to have essentially no difference with the particular ice being modeled. The resulting lognormal parameters for the bubble distribution are $r_{\mathrm{bub}} = 0.20$ mm and $s_{\mathrm{bub}} = 0.62$.

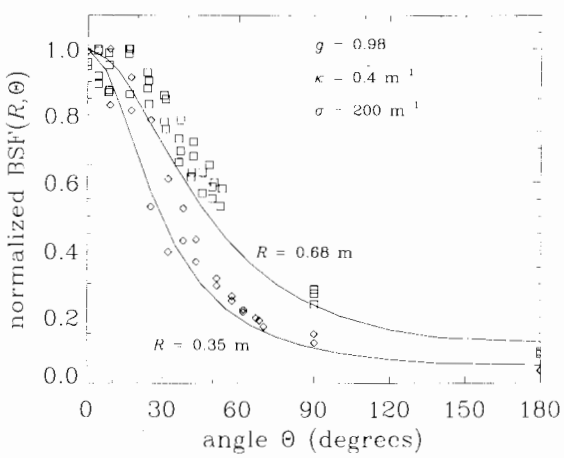

Fig. 3. Bsf's. The diamonds are measurements made with a hole separation (path length) of 0.35 m, and the squares are for 0.68 m. The solid lines are the bsf's predicted by the Monte Carlo model; note the agreement even at 180°.

The lognormal size distributions for brine pocket and air bubble radii were used as input to Mie scattering calculations of the optical absorption and scattering efficiencies and mean

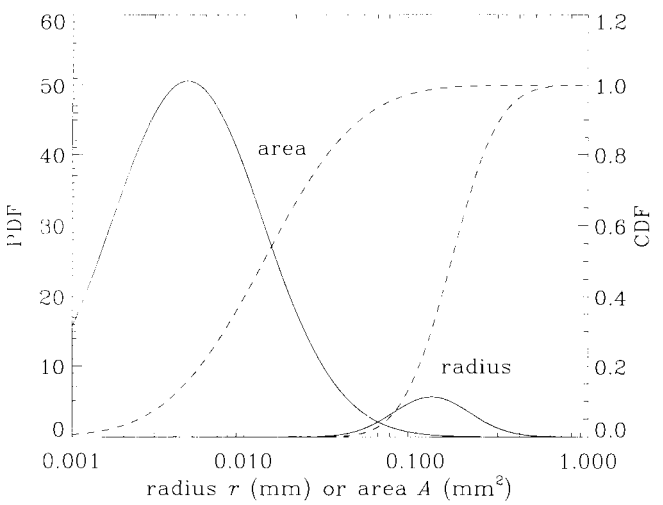

Fig. 4. Area and radius pdf's and cdf's. The solid lines show pdf(A) and pdf(r) for the parameter values used in this study. The dashed lines give the corresponding cumulative distribution functions, cdf(A) and cdf(r).

cosines of the scattering angle due to brine pockets and air bubbles. These calculations were performed in 15 bins logarithmically spaced between $s/3$ and $3s$ for each lognormal distribution. The complex indexes of refraction n = (real part, imaginary part) for pure ice and brine at 670 nm are, respectively, $(1.307,\ 2.02 \times 10^{-8})$ [8], [9] and $(1.355,\ 2.10 \times 10^{-8})$ [10], [11]. The indexes of refraction of the brine pockets and air bubbles relative to the ice itself, as used in the Mie calculations, are therefore $n_{\rm br} = (1.037,\ 4.45 \times 10^{-11})$ and $n_{\rm air} = (0.7651,\ -1.18 \times 10^{-8})$.

The absorption efficiencies $Q^{\rm abs}$ obtained from the Mie calculations are finally used with the particle size distributions $N(r)$ to compute the total absorption coefficient $\kappa_{\rm tot}$ of the ice-brine-bubble system

$$\begin{aligned}\kappa_{\rm tot} &= \kappa_{\rm ice} + \kappa_{\rm br} + \kappa_{\rm bub} \\ &= \kappa_{\rm ice} + \int Q^{\rm abs}_{\rm br}(r_{\rm br})\pi r^2_{\rm br} N_{\rm br}(r_{\rm br})\, dr_{\rm br} \\ &\quad + \int Q^{\rm abs}_{\rm bub}(r_{\rm bub})\pi r^2_{\rm bub} N_{\rm bub}(r_{\rm bub})\, dr_{\rm bub}. \end{aligned} \tag{2}$$

A corresponding equation using the scattering efficiencies gives the total scattering coefficient $\sigma_{\rm tot}$; the pure ice itself was assumed to have negligible scattering at this wavelength.

The Mie calculations also give the scattering phase functions $\tilde{\beta}(\psi)$ for the brine pockets and air bubbles; here ψ is the scattering angle. The corresponding mean cosines g of the scattering angle are obtained as the average of $\cos\psi$ when weighted by $\tilde{\beta}(\psi)$ and integrated over all scattering directions. Like κ and σ, the total volume scattering function (vsf) is the sum of the vsf's of the various components. This implies that the effective mean cosine of the scattering angle is given by

$$g = \frac{g_{\rm br}\sigma_{\rm br} + g_{\rm bub}\sigma_{\rm bub}}{\sigma_{\rm br} + \sigma_{\rm bub}} \tag{3}$$

where $g_{\rm br}$ and $g_{\rm bub}$ are the mean cosines of the scattering angles for the phase functions of the brine pockets and bubbles, respectively.

Because of the uncertainties about the brine pocket model and some of the input (such as the actual bubble concentration and size distribution), Mie calculations were performed for a range of possible conditions at site 2. These calculations show that the total absorption given by (2) is approximately 0.38 m^{-1}; this value is determined primarily by the ice itself. The total scattering coefficient varies considerably with the details of the brine pocket and bubble concentrations and size distributions; the range of predicted values for site 2 is from 175 (few bubbles) to 250 m^{-1} (many bubbles), with a likely value of around 200 m^{-1}. This σ range is consistent with previous studies [12], and a value of 200 m^{-1} gives agreement with observations in the modeling results discussed below. Most of the scattering is due to the brine pockets, and most of the variability in the total is due to the bubbles. At the temperature of the site 2 ice, the brine pockets contain only minimal amounts of $CaCO_3$ and essentially no precipitated salts, which can greatly increase the scattering if present.

The Mie calculations did not include the effects of mineral or biological particles that were imbedded in the ice. Measurement of the spectral absorption of these imbedded particles shows that they contributed at most 0.02 m^{-1} to the absorption at 670 nm. Therefore, in the modeling below, we take the total absorption at 670 nm to be $\kappa_{\rm tot} = 0.38 + 0.02 = 0.40$ m^{-1}. Imbedded particles likely contribute much less to the total scattering than the brine pockets and bubbles; we therefore keep the total scattering at $\sigma_{\rm tot} = 200$ m^{-1}.

The Mie-predicted mean cosine of the scattering angle for the brine pockets is $g_{\rm br} = 0.99$. Such a large value occurs because the brine pockets are much larger than the wavelength of the light and their index of refraction closely matches that of the ice, so that scattering is predominately by diffraction. The bubbles have $g_{\rm bub} = 0.86$. Even though the bubbles are somewhat larger than the brine pockets, their g value is smaller because the large index of refraction difference between the ice and air gives greater scattering at large angles. The effective g value given by (3) ranges from 0.96 (many bubbles) to 0.99 (few bubbles), with a likely value of around 0.98.

We assume that the scattering phase function $\tilde{\beta}(\psi)$ of the sea ice can be described by a one-term Henyey–Greenstein (OTHG) phase function

$$\tilde{\beta}(\psi) = \frac{1}{4\pi}\,\frac{1-g^2}{(1+g^2-2g\cos\psi)^{3/2}}. \tag{4}$$

Here $g = 0.98$ is the effective mean cosine of the ice-brine-bubble system, as given by (3). The inherent optical properties (IOP's) κ, σ, and $\tilde{\beta}(\psi)$ give us the information necessary for the prediction of any lightfield quantity, after imposition of appropriate boundary conditions.

IV. Prediction of BSF's

A first test of the correctness of the predicted IOP's of the ice can be made by using the IOP's to predict the bsf. Prediction of the bsf provides a particularly stringent test of the IOP's because an entire function—the shape of the bsf—must be predicted, not just a single number, as is the case, for example, with a prediction of albedo or transmission.

TABLE II
FOUR-LAYER MODEL OF THE ICE–ALGAE–WATER SYSTEM AS USED TO MODEL DAYLIGHT INTERACTIONS WITH THE SYSTEM

depth z below ice surface (m)	description	κ (m^{-1})	σ (m^{-1})	phase function
$0 \le z < 0.1$	transition ice	0.4	250	OTHG, $g = 0.95$
$0.1 \le z < 1.61$	interior ice	0.4	200	OTHG, $g = 0.98$
$1.61 \le z < 1.74$	ice + algae	1.28	200	OTHG, $g = 0.98$
$1.74 \le z < \infty$	sea water	0.5	0.1	average seawater

The θ dependence of the bsf is strongly dependent on the ψ dependence of the scattering phase function.

A Monte Carlo ray-tracing model for the simulation of point light sources in an infinite, homogeneous medium [13] was used to predict the bsf's corresponding to the measured data seen in Fig. 3. The predictions are shown as the solid lines in Fig. 3. The agreement is quite good considering the remaining uncertainties in the IOP's (in particular, the actual shape of the phase function) and the possible effects of inhomogeneities in the ice.

V. PREDICTION OF DAYLIGHT PROPAGATION

We next model the interaction of daylight with the entire ice sheet. A number of radiative transfer models are capable of simulating daylight propagation in an atmosphere–ice–water system [14]–[16]. The model we use here is the Hydrolight radiative transfer model [16], [17]. Hydrolight solves the radiative transfer equation from first principles using invariant imbedding methods to obtain the spectral radiance distribution as a function of depth, direction, and wavelength throughout and leaving the medium. The model can accept as input any depth profile of IOP's and any incident sky radiance distribution. Both rough and smooth sea or ice surfaces can be simulated. Quantities such as irradiances, albedos, or diffuse attenuation functions are obtained from their definitions after the radiance distribution is computed. To employ this or any other such model, we must first specify appropriate IOP's and boundary conditions for the system.

The IOP's predicted by the Mie calculations and used above for the beam spread modeling apply only to the interior region of the ice sheet. Although some banding could be seen in ice cores, indicating at least some variability with depth in the IOP's, measured temperature, salinity, and density profiles [2, Fig. 5] are fairly constant throughout the interior of the ice sheet. Moreover, the Mie calculations were based on parameter values taken from the midrange of values found within the ice interior. We therefore assume that the IOP's computed above are valid for the interior of the ice, namely, from a depth of 0.1–1.6 m. However, very near the ice surface and bottom there were thin layers that differed considerably from the ice interior in their optical properties. These IOP's of these layers should be modeled separately, even if approximately.

Near the ice surface, there was a 0.1-m-thick layer of fine-grained transition ice that had an air content of 3.9–4.1%, in contrast to values between 0.5 and 1% (averaging about 0.8%) within the interior of the ice sheet. This transition layer likely will have a higher scattering coefficient σ and lower g because of the higher number of bubbles. We did not perform Mie calculations for this layer. However, simply assuming that the contribution by bubbles to the total scattering increases by a factor of 4.0%/0.8% = 5 over the contribution by bubbles deeper within the ice gives $\sigma = 250\ m^{-1}$ within the transition layer. Equation (3) yields $g = 0.95$. The absorption, which is due primarily to the ice, is kept at $\kappa = 0.4\ m^{-1}$.

The bottom surface of the ice contained a dense algae mat approximately 1 cm thick, with some algae distributed throughout the bottom few centimeters of the ice. The absorption coefficient due to algae and dissolved matter as measured on the bottom 13 cm of an ice core (from depth 1.61 to 1.74 m) averaged $0.90\ m^{-1}$. Adding this value to the absorption by the ice itself ($0.38\ m^{-1}$) gives a total average absorption of $\kappa = 1.28\ m^{-1}$ within the layer. The increase in scattering due to the algae was not measured, but it is likely small compared to the scattering caused by the brine pockets and air bubbles; we therefore keep $\sigma = 200\ m^{-1}$ in this layer. Since the actual profile of absorption within this layer was not measured, we model the algae effects simply as a homogeneous layer between 1.61 and 1.74 m, having the average κ and assumed σ values; the value of g is kept at 0.98.

The IOP's of the water below the ice were not measured. We therefore use $\kappa = 0.5\ m^{-1}$ and $\sigma = 0.1\ m^{-1}$, along with a typical seawater phase function [17, Table 3.10, column 6], as reasonable estimates of the water IOP's. The water below the ice was taken to be optically infinitely deep. We now have in hand a simple, four-layer IOP model of the ice–algae–water system, which is summarized in Table II.

Because no data (other than visual inspection) were available on the small-scale roughness of the air–ice surface, the air–ice surface was taken to be somewhat rough via the artifice of using Cox–Munk capillary wave slope statistics for a wind speed of 15 ms^{-1} to model the radiance reflection and transmission properties of the ice surface. The sky was assumed to have a cardioidal radiance distribution, which is typical of a heavily overcast day. These surface boundary conditions give us the remaining information needed to run Hydrolight.

Hydrolight was run with the IOP's and boundary conditions just specified. The albedo of the ice–water system,

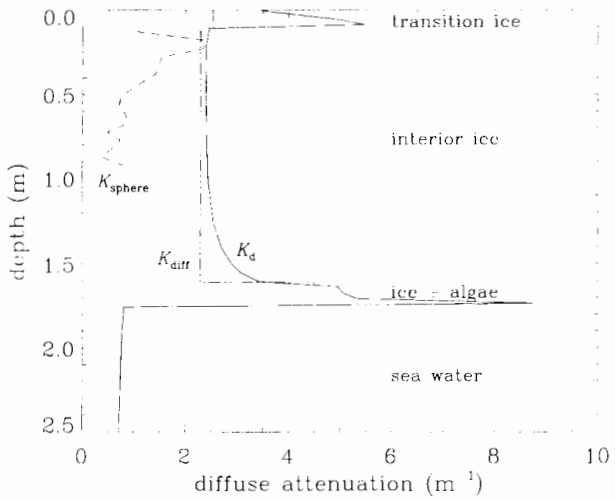

Fig. 5. Depth profiles of diffuse attenuation functions. The solid line is K_d, as computed by Hydrolight using the IOP's of Table II. The dashed line is the measured $K_{\rm sphere}$. The dash-dot-dot line is K, as given by diffusion theory (7) for the IOP's of the ice.

the irradiance transmission through the ice, and the diffuse attenuation profile K_d within the ice were computed from the radiance distribution for comparison with measured values. The albedo measured in the field was $A = 0.48$; the value predicted by Hydrolight was 0.44. In the present simulation, the computed value of E_d at $z = 1.75$ m was used to compute the transmission T through the ice. The measured T was 0.01; the predicted value was 0.0094. For both A and T, the measured and predicted values agree to within 8%, which is in agreement considering the crudeness of the IOP model. If the entire 1.74-m ice layer is modeled with the IOP's of the interior ice, the albedo decreases to 0.34 and the transmission increases to 0.015; these larger disagreements with observation highlight the importance that even relatively thin layers can have on optical propagation, if the layers have IOP's that are significantly different from the main body of the ice. Likewise, the roughness of the air–ice surface affects the albedo and transmittance. If the ice surface is modeled as being perfectly flat (which it was not), for example, the albedo decreases to 0.37 and the transmittance increases to 0.011. The surface roughness is thus seen to have a possible influence on the albedo and transmittance that is comparable to that of the thin surface and bottom layers; the surface-roughness effect would be even larger for clear skies and low solar elevations.

The solid line in Fig. 5 shows the depth profile of the diffuse attenuation function for downwelling plane irradiance

$$K_d(z) = -\frac{1}{E_d(z)}\frac{dE_d(z)}{dz}. \tag{5}$$

It should be noted that, although we are using four homogeneous layers to model the IOP's, Hydrolight can compute depth profiles of the radiance distribution and derived quantities with any desired depth resolution; its output is not simply layer-averaged values. The K_d profile shown in Fig. 5 was computed using $\Delta z = 0.01$ m in a finite-difference approximation of (5). This is much higher resolution than can be realized in the field, where a Δz of 0.1 m or greater is typical. Using a larger Δz smooths out the spikes in K_d that occur at the boundaries between layers with greatly different IOP's. The dashed line in Fig. 5 shows the diffuse attenuation $K_{\rm sphere}$ measured by the 13-cm-diameter diffusing sphere described in the data section. The values of $K_{\rm sphere}$ would not be equal to K_d near a boundary because the instrument geometries are different. However, when optically far away from boundaries, these two K functions should both nearly equal the asymptotic value K_∞, which is 2.4 m^{-1} for the IOP's of the interior ice. (K_∞ was computed using an eigenmatrix method described in [17, Sec. 9–6]) The value of K_d agrees with K_∞ in the middle of the ice layer, indicating that the light field is nearly asymptotic. However, $K_{\rm sphere}$ averages about 0.7 m^{-1} at depths from 0.5 to 0.9 m, considerably less than the anticipated value of 2.4 m^{-1}. The reason for this discrepancy is not known. However, the measured $K_{\rm sphere}$ would be less than its true value if sky light were able to enter the hole into which the instrument was inserted and then to scatter through the ice and around the light baffles, which were intended to shield the diffusing sphere from the ambient light in the hole above it. We note that the average K_d value for the entire 1.74-m ice layer corresponding to the measured irradiance transmission of 0.01 is 2.6 m^{-1}. This value is consistent with the detailed K_d profile seen in Fig. 2. K values in the range of 2–4 m^{-1} are typical of young white ice [11], [18].

VI. Diffusion Theory

Several recent studies [7], [19]–[21] have pointed out the utility of diffusion theory for modeling some aspects of light propagation in sea ice. According to diffusion theory, all light-field quantities decay with depth at a rate given by

$$K_{\rm diff} = (\kappa + \sigma)\sqrt{3[1 - \omega_o - g\omega_o(1 - \omega_o)]} \tag{6}$$

where $\omega_o = \sigma/(\kappa + \sigma)$ is the albedo of single scattering. Inserting the predicted IOP's for the interior of the ice into (6) gives $K_{\rm diff} = 2.3$ m^{-1}. This agreement with the value of $K_\infty = 2.4$ m^{-1}, just discussed, indicates that diffusion theory is probably adequate for modeling daylight propagation in the interior of the ice. However, diffusion theory is valid only when optically far from boundaries. Note in Fig. 5 that, even when (6) is evaluated with the IOP's of the transition and algae layers, $K_{\rm diff}$ differs considerably from K_d near the air–ice and ice–water boundaries. Diffusion theory therefore cannot be expected to adequately model the albedo of the ice, for example, which is largely determined by light scattering near the air–ice surface.

VII. Conclusions

The general agreements between predictions and observations obtained in this exercise indicate that the modeling tools now available are capable of predicting light propagation in sea ice with considerable accuracy. In particular, we have shown that it is possible to begin with the physical properties of sea ice and to carry through to the prediction of various optical quantities of interest in remote sensing, ice thermodynamics, and biological productivity. Any doubts about this process arising from philosophical concerns about the applicability of Mie theory to nonspherical brine pockets, or about the

applicability of classical radiative transfer theory to light propagation in sea ice, appear to be unfounded.

Given our confidence in these forward models, we also can employ them as the core of implicit inverse models. Such models attempt to extract information about the ice IOP's from measured lightfield quantities by solving a sequence of forward problems as the input IOP's are varied and the model predictions are compared with observation. We do note, however, that it is important to have the largest possible suite of lightfield measurements when attempting such inversions. It is possible, for example, to obtain IOP's that correctly predict the albedo and transmittance, but which fail to predict the shape of the bsf, or vice versa. The EMPOSI field experiment showed that it is possible to obtain a comprehensive optical data set, which can greatly constrain the possible solutions of such inversions.

REFERENCES

[1] K. C. Jezek, D. K. Perovich, K. M. Golden, C. Luther, D. G. Barber, P. Gogineni, T. C. Grenfell, A. K. Jordan, C. D. Mobley, S. V. Nghiem, and R. G. Onstott, "A broad spectral, interdisciplinary investigation of the electromagnetic properties of sea ice," this issue, pp. 1633–1641.

[2] D. K. Perovich and A. J. Gow, "A quantitative description of sea ice inclusions," *J. Geophys. Res.*, vol. 101, no. C8, pp. 18 327–18 343, 1996.

[3] D. K. Perovich, J. Longacre, D. G. Barber, R. A. Maffione, G. F. Cota, C. D. Mobley, A. J. Gow, R. G. Onstott, T. C. Grenfell, W. S. Pegau, M. Landry, and C. S. Roesler, "Field observations of the electromagnetic properties of first-year sea ice," this issue, pp. 1705–1715.

[4] B. G. Mitchell, "Algorithms for determining the absorption coefficient of aquatic particulates using the quantitative filter technique (QFT)," in *Proc. SPIE, Ocean Opt. X*, R. W. Spinrad, Ed. 1990, vol. 1302, pp. 137–148.

[5] A. Bricaud, A. Morel, and L. Prieur, "Absorption by dissolved organic matter of the sea (yellow substance) in the UV and visible domains," *Limnol. Oceanogr.*, vol. 26, no. 1, pp. 43–53, 1981.

[6] L. E. Mertens and F. S. Replogle, Jr., "Use of point and beam spread functions for analysis of imaging systems in water," *J. Opt. Soc. Amer.*, vol. 67, no. 8, pp. 1105–1117, 1977.

[7] R. A. Maffione and C. D. Mobley, "Theory and measurements of the complete beam spread function of sea ice," *Limnol. Oceanogr.*, vol. 43, no. 1, pp. 34–43, 1998.

[8] T. C. Grenfell and D. K. Perovich, "Radiation absorption coefficients of polycrystalline ice from 400–1400 nm," *J. Geophys. Res.*, vol. 86, no. C8, pp. 7447–7450, 1981.

[9] S. G. Warren, "Optical constants of ice from the ultraviolet to the microwave," *Appl. Opt.*, vol. 23, pp. 1206–1225, 1984.

[10] G. A. Maykut and B. Light, "Refractive-index measurements of freezing sea-ice and sodium chloride brines," *Appl. Opt.*, vol. 34, pp. 950–961, 1995.

[11] T. C. Grenfell, "A theoretical model of the optical properties of sea ice in the visible and near infrared," *J. Geophys. Res.*, vol. 88, no. C14, pp. 9723–9735, 1983.

[12] D. K. Perovich, "The optical properties of sea ice," Mono. 96-1, U.S. Army Cold Reg. Res. Eng. Lab., Hanover, NH, 1996, p. 25.

[13] C. D. Mobley, "Monte Carlo simulation of a point light source in an infinite medium," SRI Int., Menlo Park, CA, Tech. Rep., SRI Project 7311, 1996, p. 39.

[14] Z. Jin, K. Stamnes, W. F. Weeks, and S.-C. Tsay, "The effect of sea ice on the solar energy budget in the atmosphere-sea ice-ocean system: A model study," *J. Geophys. Res.*, vol. 99, no. C12, pp. 25 281–25 294, 1994.

[15] T. C. Grenfell, "A radiative transfer model for sea ice with vertical structure variations," *J. Geophys. Res.*, vol. 96, no. C9, pp. 16 991–17 001, 1991.

[16] C. D. Mobley, B. Gentili, H. R. Gordon, Z. Jin, G. W. Kattawar, A. Morel, P. Reinersman, K. Stamnes, and R. H. Stavn, "Comparison of numerical models for computing underwater light fields," *Appl. Opt.*, vol. 32, no. 36, pp. 7484–7504, 1993.

[17] C. D. Mobley, *Light and Water: Radiative Transfer in Natural Waters*. San Diego, CA: Academic, 1994.

[18] T. C. Grenfell and G. A. Maykut, "The optical properties of ice and snow in the Arctic basin," *J. Glaciol.*, vol. 18, no. 80, pp. 445–463, 1977.

[19] C. D. Mobley and R. A. Maffione, "Effects of absorption and boundary conditions on the utility of diffusion theory," in *Proc. SPIE, Ocean Optics XIII*, S. G. Ackleson and R. Frouin, Ed. 1997, vol. 1963, pp. 16–20.

[20] R. A. Maffione, "Theoretical developments on the optical properties of highly turbid waters and sea ice," *Limnol. Oceanogr.*, vol. 43, no. 1, pp. 29–33, 1998.

[21] C. D. Mobley and R. A. Maffione, "The utility of first-order diffusion theory for modeling light propagation in sea ice," submitted for publication.

Curtis D. Mobley, photograph and biography not available at the time of publication.

Glenn F. Cota, photograph and biography not available at the time of publication.

Thomas C. Grenfell (M'94–A'95), for a photograph and biography, see p. 124 of the January 1998 issue of this TRANSACTIONS.

Robert A. Maffione, photograph and biography not available at the time of publication.

W. Scott Pegau, photograph and biography not available at the time of publication.

Donald K. Perovich, for a photograph and biography, see p. 124 of the January 1998 issue of this TRANSACTIONS.